Energy, Environmental, and Catalysis Applications

Weak Intermolecular Interactions in Covalent Organic Framework-Carbon Nanofiber based Crystalline, Yet Flexible Devices

Abdul Khayum Mohammed, Vidyanand Vijayakumar, Arjun Halder, Meena Ghosh, Matthew Addicoat, Umesh Pandharinath Bansode, Sreekumar Kurungot, and Rahul Banerjee

ACS Appl. Mater. Interfaces, **Just Accepted Manuscript** • DOI: 10.1021/acsami.9b08625 • Publication Date (Web): 06 Aug 2019

Weak Intermolecular Interactions in Covalent Organic Framework-Carbon Nanofiber based Crystalline, Yet Flexible Devices

Abdul Khayum Mohammed,[a, b] Vidyanand Vijayakumar,[a, b] Arjun Halder,[a, b] Meena Ghosh,[a,b] Matthew Addicoat,[c] Umesh Bansode,[d] Sreekumar Kurungot,[a, b] Rahul Banerjee[e]*

[a]Academy of Scientific and Innovative Research, CSIR- Human Resource Development Centre, (CSIR-HRDC) Campus, Ghaziabad, Uttar Pradesh- 201 002, India.

[b]Physical/ Materials Chemistry Division, CSIR-National Chemical Laboratory, Dr. Homi Bhabha Road, Pune-411008, Maharashtra, India.

[c]School of Science and Technology, Nottingham Trent University, Clifton Lane, NG11 8NS Nottingham, United Kingdom.

[d]Department of Physics, Indian Institute of Science Education and Research, Pune Dr. Homi Bhabha Road, Pune-411008, Maharashtra, India.

[e]Department of Chemical Sciences, Indian Institute of Science Education and Research, Kolkata, Mohanpur 741246, West Bengal, India.

KEYWORDS: covalent organic frameworks, electrical conducting materials, flexible supercapacitors, self-charging power-packs, redox-active porous materials, multi-functional materials

ABSTRACT

The redox-active and porous structural backbone of covalent organic frameworks (COFs) can facilitate high-performance electrochemical energy storage devices. However, the utilities of such 2D-materials as supercapacitor electrodes in advanced self power-pack systems have been obstructed due to the poor electrical conductivity and subsequent indigent performance. Herein, we report an effective strategy to enhance the electrical conductivity of COF thin sheets through the *in situ* solid-state inclusion of carbon nanofiber (CNF) into the COF precursor matrix. The obtained COF-CNF hybrids possess a significant intermolecular π•••π interaction between COF and the graphene layers of the CNF. As a result, these COF-CNF hybrids (**DqTp-CNF** and **DqDaTp-CNF**) exhibit good electrical conductivity (0.25×10^{-3} Scm^{-1}), as well as high performance in electrochemical energy storage (**DqTp-CNF:** 464 $mFcm^{-2}$at 0.25 $mAcm^{-2}$). Also, the fabricated, mechanically strong quasi-solid-state supercapacitor (**DqDaTp-CNF SC**) delivered an ultra-high device capacitance of 167 $mFcm^{-2}$ at 0.5 $mAcm^{-2}$. Furthermore, we integrated a monolithic photovoltaic self-charging power-pack by assembling **DqDaTp-CNF SC** with a perovskite solar cell. The fabricated self power-pack delivered excellent performance in the areal capacitance (42 $mFcm^{-2}$) at 0.25 $mAcm^{-2}$ after photo charging for 300 seconds.

Introduction

Covalent organic frameworks (COFs) are two-or-three-dimensional (2D/3D) crystalline ordered network structures constructed from purely organic building blocks.[1-11] These structurally pre-defined nano-materials bearing high surface area and redox-active functionalities have emerged as outstanding electrodes in electrochemical energy storage devices.[12-16] However, their insignificant electrical conductivity, or mostly insulating behavior, greatly hinders the utilization of COFs as energy storage devices.[17] Moreover, the nano-crystalline nature of COFs with several grain boundaries or defects heavily prevent the smooth flow of electrons among the crystallites and could be a road-block towards the facile fabrication of free-standing flexible supercapacitors. Notably, there have been a few attempts to enhance the electrical conductivity of COFs *via ex situ* loading of conducting polymers within the COF backbone.[18-19] Moreover, the research on the COF-carbon nanotube based composites results in improved charge storages in batteries by the enhancement of the electrical conductivity of the electrode.[20-21] However, the design and construction of a COF free-standing thin sheet with excellent electrical conductivity is still an under-explored area and requires significant scientific attention.

Keeping all these in perspective, herein, we have detailed a novel synthetic method to load electrically conducting carbon nanofiber (CNF) [22] into the COF matrix, using an *in situ* solid-state mechano-mixing technique.[23] The numerous π-electrons in the COF backbone aid weak intermolecular π•••π interactions with the sp^2 graphene carbons of CNF as evidenced from density functional tight binding (DFTB) calculations.[24-30] Due to these inter-molecular interactions, the COF-CNF hybrids promote efficient electron transfer through the matrix. Subsequently, the resulting COF-CNF hybrids exhibit more than 10^9 fold increment in the electrical conductivity (0.25×10^{-3} Scm^{-1}) compared to the pristine COFs. Again, these

intermolecular interactions in COF-CNF induce a free-standing nature, as well as flexibility among the COF-CNF hybrid devices. Additionally, these hybrids could maintain their crystallinity and overall porosity (472 and 532 m^2g^{-1}) compared to the pristine COFs. We have loaded only 20% CNF (20 mg CNF/100 mg of precursors) within the COF matrix to preserve the porosity and the number of redox-active sites per unit volume, which also maintains the mechanical robustness of the hybrid.

We have selectively chosen two different *β*-ketoenamine[31] based 2D-COFs as the active materials for the COF-CNF hybrid preparation: 1) **DqTp**, a COF with an anthraquinone backbone (anthraquinone has already been tested as an active redox center);[12] 2) **DqDaTp**, a COF with an anthraquinone-anthracene based hetero-linked backbone (to bring in enough flexibility to the composite).[32] The excellent areal capacitance of 464 $mFcm^{-2}$ for the **DqTp-CNF** hybrid in contrast to the 38 $mFcm^{-2}$ capacitance of pristine **DqTp** indicates the influence of electrical conductivity on the overall capacitance value. Moreover, we believe that the enhanced electrical conductivity of the COF-CNF hybrid electrode improves the efficacy of the electron transfer *via* both Faradaic and non-Faradaic processes. Although **DqTp** could serve as a rich redox-active platform, in the current scenario, we have strategically used the hetero-linked **DqDaTp-CNF** hybrid for the final device fabrication because of its good redox activity, in addition to excellent mechanical robustness (5.8% breaking strain compared to the 1.2% breaking strain of **DqTp COF**). Therefore, we could construct a flexible supercapacitor device with the **DqDaTp-CNF** hybrid that exhibits an areal capacitance as high as 167 $mFcm^{-2}$. To the best of our knowledge, the device capacitance value, in the present study, is one of the best reported areal capacitances among the COFs; MOFs; and several other carbon-based supercapacitors.[33-38] Furthermore, it could deliver an excellent energy density of 5.8 $\mu Whcm^{-2}$,

which suggested to us that we could integrate a photo-voltaic charged supercapacitor-solar cell device,[39-42] for its further implementation towards concurrent harvest and energy storage.

Experimental Section

COF-CNF hybrid thin sheet fabrication:

DqTp-CNF hybrid: *2,6*-diaminoanthraquinone (**Dq**, 0.6 mmol) and *p*-toluenesulphonic acid (**PTSA,** 3 mmol) were thoroughly mixed at room temperature and 100 µl of water was added to the system. To the homogeneous mixture *1,3,5*-triformylphloroglucinol (**Tp**, 0.4 mmol) was added and again mixed vigorously for 10 minutes. Finally, carbon nanofiber (20 wt% of the precursors- amine and aldehyde) was added to the obtained mixture and then thoroughly mixed for 1 minute until getting a black colored paste. This paste was then coated on a 2.5 × 8 cm^2 glass surface by using a glass slide to form a uniform thin sheet and heated to 120°C for 24 hours under closed condition (The thickness of the COF-CNF thin sheet can be controlled by varying the area of the glass surface). Later, the COF-CNF thin sheet was taken from glass slide by dipping in distilled water and washed by the following order with water, *N,N*-dimethylacetamide, water and acetone (Isolated yield: 90%) (Figure 1c; S-2, Supporting Information).

DqDaTp-CNF hybrid: The two amines [*2,6*-diamino anthracene (**Da**) and *2,6*-diamino anthraquinone (**Dq**)] were taken (totally 0.6 mmol) in 1:1 ratio and mixed well to make it a uniform mixture. Then **PTSA** (3 mmol) was added and thoroughly mixed for 5 minutes at ice bath temperature. After the addition of 100 µl of water, *1,3,5*-triformylphloroglucinol (**Tp**, 0.4 mmol) was added to the mixture. Finally, carbon nanofiber (20 wt% of the precursors- amine and aldehyde) was added to the obtained mixture and then thoroughly mixed for 1 minute until getting a black colored paste. This paste was then coated on a 2.5 × 8 cm^2 glass surface by using a glass slide to form a uniform thin sheet and heated to 120°C for 24 hours under closed

condition. Later, the COF-CNF thin sheet was taken from glass slide by dipping in distilled water and washed by the following order with water, *N,N*-dimethylacetamide, water and acetone (Isolated yield: 85-90%) (Figure 1c; S-2, Supporting Information).

Three-electrode assembly: The COF-CNF hybrid thin sheets (1 cm^2 geometrical area) with a thickness of 50 μm were taken as working electrodes. Then the COF-CNF thin sheet is dipped in 1M H_2SO_4 for1 hour for the activation of pores and the improvement of electrode-electrolyte interaction. In the three-electrode system, the Pt, and Hg/Hg_2SO_4 were used as the counter electrode and the reference electrode respectively in 1M H_2SO_4 electrolyte. The COF-CNF thin sheets were directly attached to the crocodile clip with the help of a small piece of grafoil for the better electrical contact with the metallic-clip (S-10, Supporting Information).

Device fabrication: The symmetric supercapacitor device was fabricated by taking 1 cm^2 geometrical area of **DqDaTp-CNF** COF as electrodes. These COF electrodes were placed on the grafoil sheets which have been served as a current collector of the supercapacitor. A thin layer of PVA-H_2SO_4 electrolyte gel was uniformly coated on COF-CNF thin sheet and allowed to wet the electrode completely. Two electrodes were made by the aforementioned procedure and these two electrodes were sandwiched by keeping a polypropylene separator in between them(S-10, Supporting Information).

Results and Discussion

Here, we tried to fabricate COF-CNF hybrids with varying percentages of CNF loading (10% and 20%). Since the COF-CNF-20% hybrid exhibits higher charge storage performance, in the present work, we have focused on the structure and properties of **DqTp-CNF** and **DqDaTp-CNF** with 20% CNF loading. Due to the higher mechanical robustness, **DqDaTp-CNF-20%**

(which will be addressed as **DqDaTp-CNF** in the rest of the paper**)** has been integrated as a flexible supercapacitor and then as a photo-voltaic charged supercapacitor-solar cell device.

The structural elucidation of the COF-CNF hybrids, reported in this paper, has been resolved using powder X-ray diffraction analysis (Figure 1a, b, d & e). The **DqTp-CNF** hybrid features a crystalline pattern with a prominent 100 peak and a broad 001 peak at 3.6° and 26-27° (2*θ)* respectively. Similarly, the **DqDaTp-CNF** hybrid also exhibits a crystalline PXRD pattern with 100 and 001 reflections at 3.4°and 27° (2*θ*) respectively. Notably, both experimental PXRD profiles match with the simulated honeycomb 2D lattice eclipsed structure. Moreover, in addition to the characteristic COF peaks, a sharp peak attributed from 002 plane reflection at 26-27° (2θ) present in both PXRD patterns indicates the presence of CNF in the COF-CNF hybrids(Supporting Information, Figure S2-S3). However, it is observed that the sharp 002 peak is shifted towards the lower 2θ angle in the composite, compared to the pristine CNF (Figure 1b & e). This peak shift could be due to the inter-space widening of the 002 planes of the CNF resulting from the interlayer COF-CNF interactions. We have used the herringbone cup-stacked hollow CNF with a fiber axial angle of 30°. Moreover, owing to the specific structural features of these CNFs (Supporting Information, Figure S49), [22] the *in situ* hybrid synthesis allows an effective growth of respective COF crystallites inside as well as outside walls of the nanofibers. The large (~100 nm) open aperture of the CNF structure can provide the space for the successful growth of COF crystallites inside the large hollow central core of the CNF (70-80 nm). While, on the outer wall, due to the large lateral dimension, the curvature of the graphene layers of the conical shape CNF is very negligible and becomes almost planar, which makes them a good platform for the COF growth. A similar COF growth, when attempted, is not observed in the case of the COF-carbon nanotube (COF-CNT) composite due to the small lateral dimension

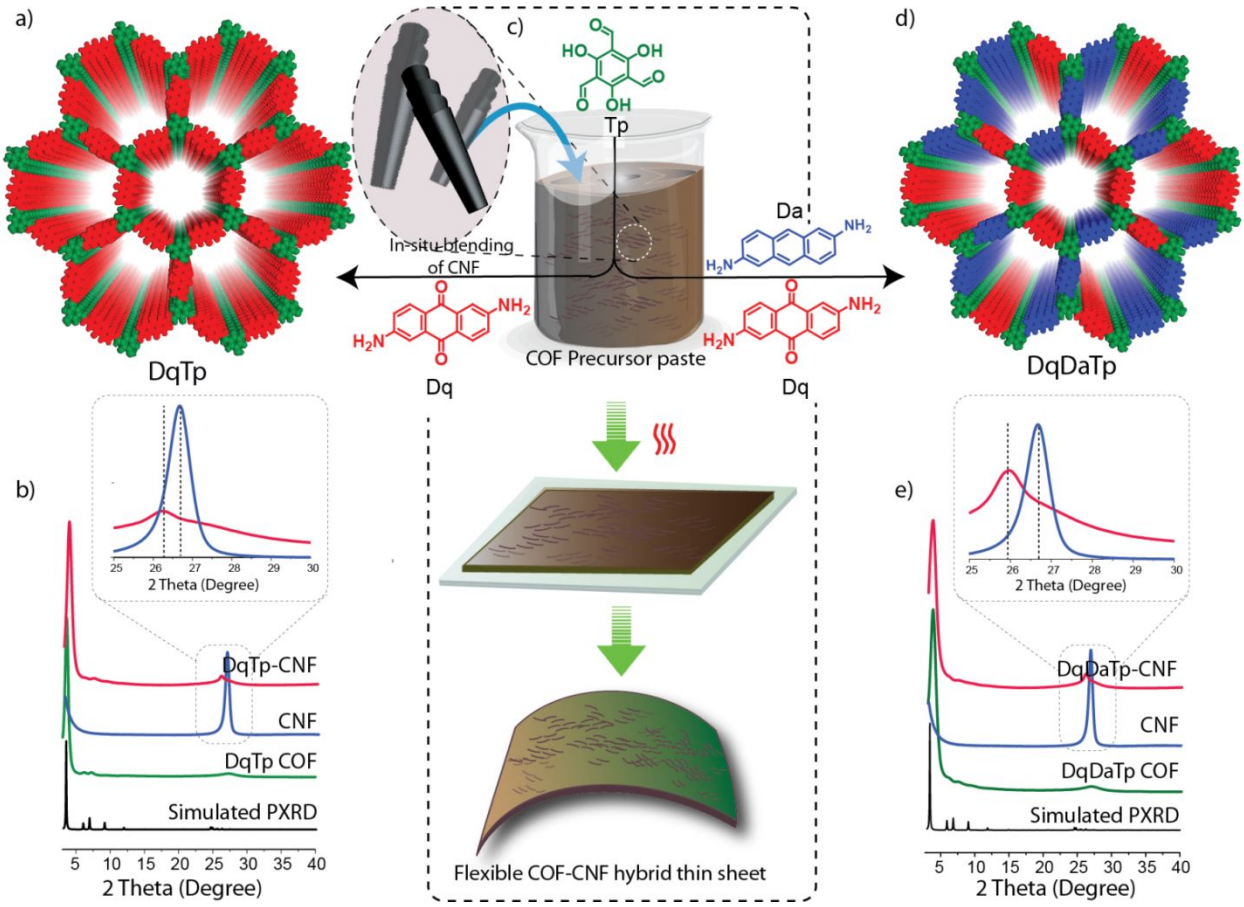

Figure 1: a & d) Eclipsed model of **DqTp** and **DqDaTp** COFs; b & e) PXRD patterns of **DqTp-CNF** and **DqDaTp-CNF** hybrids; c) Schematic representation of the synthesis of crystalline yet flexible **DqTp-CNF** and **DqDaTp-CNF** COFs.

(diameter- ~20 nm) and the large cylindrical curvature of the CNTs. The weak intermolecular π•••π interaction between COF and CNT is not effective as a COF-CNF hybrid (Supporting Information, Figure S21 & S50) which further leads to the fragility of the COF-CNT based hybrids.

The formation of the *β*-ketoenamine based chemical structure in **DqTp-CNF** and **DqDaTp-CNF** hybrids is clearly indicated by the respective C–N (1225 & 1216 cm^{-1}) and C=O bonds (1663 & 1667 cm^{-1}) stretching vibrations in the FTIR spectrum. The characteristic stretching

vibrations of the anthraquinone keto group (C=O) appeared at 1663 and 1667 cm^{-1} for the respective COFs (Supporting Information, Figure S13-S15). The atomic level construction of the COF-CNF hybrids is further investigated by ^{13}C CP MAS solid-state NMR spectroscopy. The characteristic keto peak from *β*-ketoenamine COF resonance appears at 183-184 ppm whereas the enamine carbon exhibits peaks at 147 and 145 ppm for **DqTp-CNF** & **DqDaTp-CNF** respectively (Supporting Information, Figure S16). The TGA profiles exhibit significant thermal stability of COF-CNF thin- sheets up to 430°C (Supporting Information, Figure S17). However, the slight weight loss of COF-CNF hybrids in the temperature range of 200-400° C in the TGA profile could be due to the decomposition of the oligomers were trapped inside the COF matrix. The COF-CNF hybrids maintained their overall porous nature, unlike many other COF composite materials reported in the literature.[43-45] The BET surface areas of **DqTp-CNF** and **DqDaTp-CNF** hybrids were calculated as 472 and 532 m^2g^{-1} respectively (Supporting Information, Figure S18). The uniform pore diameter of ~2.2 nm for both COF-CNF hybrids, calculated using the non-local density functional theory (NLDFT), further suggest the existence of a well-organized framework structure (Supporting Information, Figure S19).

To obtain fundamental insights about the interlayer interactions that reported here, we have modeled the possible structure of COF-CNF hybrids using DFTB. The herringbone/cup-stacked CNF is generally made up of slightly curved graphene layers (30° fiber axial cone angle with an open aperture of 70-80 nm diameter). Taking this into consideration, initially, we optimized different models of COF-planar graphene systems in both vacuum and non-vacuum modes. As **DqDaTp** (1:1) exhibits a large asymmetric unit, we have specifically focused on similar hetero-linked COFs such as **Dq_1Da_2Tp** (1:2) and **Dq_2Da_1Tp** (2:1) and homo linked **DqTp** and **DaTp** (anthracene) COFs for corresponding DFTB modeling (Supporting Information, Figure S5). We

have optimized different multilayer sets of all COF-planar graphene systems such as 2-2-2 [two graphene -two COF -two graphene layers] and 3-3-3 [three graphene -three COF -three graphene layers] models to quantify the perlayer stabilization energy and to determine the nature of the interaction among the layers (Figure 2 a-d; Supporting Information, Figure S6-S11, Table S1). The COF-graphene monolayer optimized structure suggests that the COF stacks on the graphene in a slightly shifted arrangement on the corresponding 002 plane of the graphene layers (Supporting Information, Figure S6). Additionally, these calculations also suggest a three-fold increment in the perlayer stabilization energy of the COF-planar graphene system compared to the pristine COFs. In the 2-2-2 mode, the estimated perlayer stabilization energy (~295 kcalmole^{-1}) of all COF-planar graphene systems is significantly higher compared to the perlayer stabilization energies for a pristine COF (only 80-83 kcalmole^{-1}). Similarly, enhanced perlayer stabilization energy (~335 kcalmole^{-1}) is also observed in the 3-3-3 mode. Considering a fully periodic (no-vacuum in the *c*-direction) calculation, a higher perlayer stabilization energy (~420 kcalmole^{-1}) for the similar 3-3-3 system was obtained which indicates that perlayer stabilization is dominated by the graphene-graphene interactions. Furthermore, the DFTB analysis indicates a compression in the COF-COF (3.36 Å to 3.31-3.21 Å) and COF-graphene (3.21 Å) interplanar distances among these hybrids.[46-47] Such observation, in turn, reflects an improved and efficient stacking interaction between the COF and graphene planes. As a result, the interplanar distance of graphene-graphene layers noticeably widened in both systems (~3.41 Å) compared to the pristine graphene model (3.36 Å), which indicates a weakening of the π•••π stacking between the graphene layers (Figure 2c, d & e). Additionally, to present a more realistic model of the COF-CNF hybrid, we have optimized the DFTB models of a COF-curved graphene system considering armchair the (AC) configuration in the vacuum condition

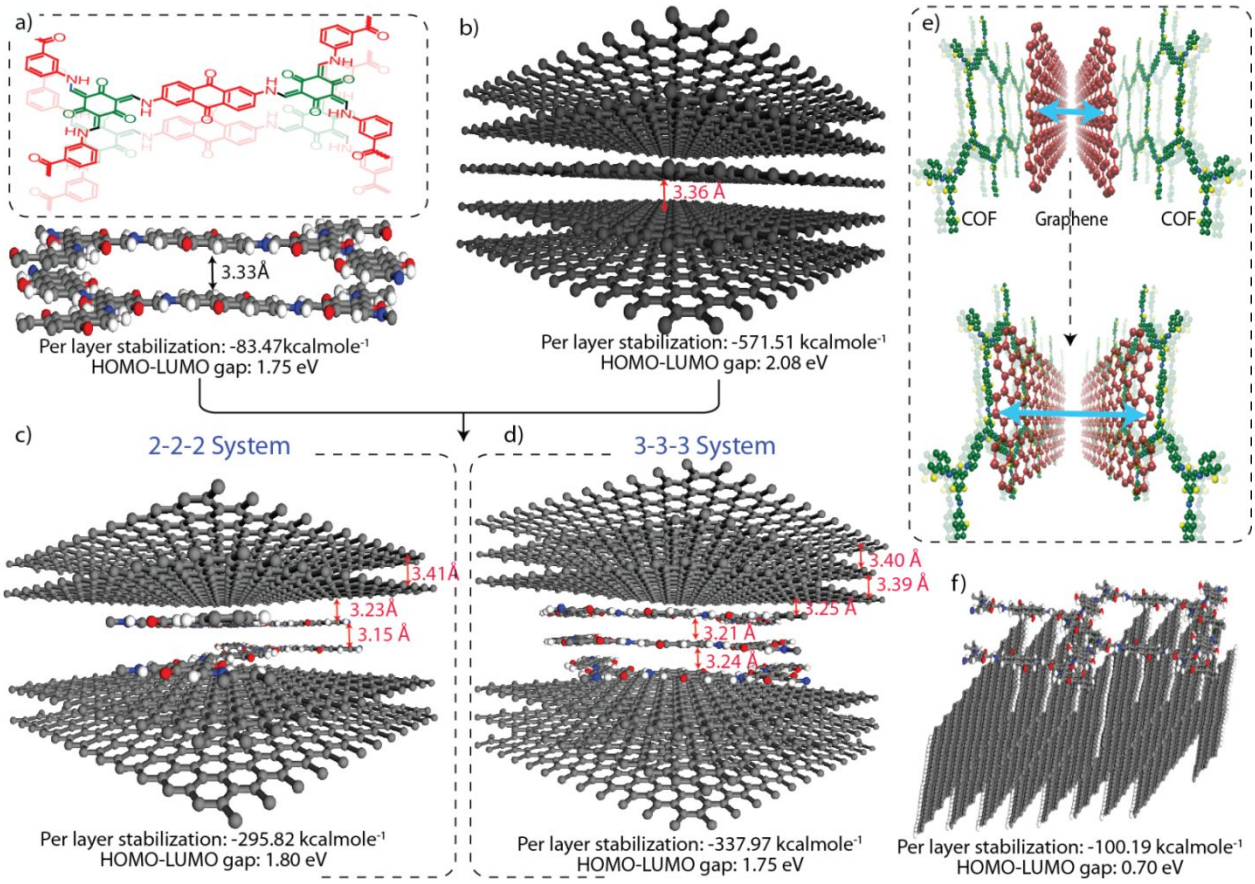

Figure 2: The DFTB model structure of a) **DqTp** COF; b) graphene; c) COF-planar graphene 2-2-2 system vacuum mode; d) COF-planar graphene 3-3-3 system vacuum mode; e) The diagrammatic representation of the interlayer interaction of COF-graphene model; f) The COF stacked on the vertically aligned curved graphene.

(Supporting Information, Figure S12). Herein, we have considered a stacking model where the COF stacked on the top of the vertically aligned curved graphene planes. The enhancement of stabilization energy (~105 kcalmole^{-1}layer^{-1}) compared to the pristine COF models (80-84 kcalmole^{-1}layer^{-1}) has been observed in these COF-curved graphene systems. As the curvature of graphene layers in CNF compared to the planar graphene is quite negligible, both the COF-planar graphene and COF-curved graphene models are considered as possible structures of the hybrid system.

The peak shifts in the X-Ray photoelectron spectroscopy (XPS) of the COF-CNF hybrids from the pristine COFs indicate the origin of new electronic interactions in the COF-CNF

hybrids (Figure 3a and b).[48-51] The XPS after the deconvolution shows the pristine CNF and **DqDaTp** display the C1s peak at 284.5 and 284.8 eV respectively (Supporting Information, Figure S26). However, the XPS profile of the **DqDaTp-CNF** hybrid shows a C1s peak at 285.9 eV. Therefore, we believe, the higher binding energy shift in the COF-CNF hybrid compared to the pristine COF and CNF, indicates the interlayer π•••π interaction between the COF and the CNF. Similarly, the XPS C1s profile of **DqTp-CNF** at ~285.1 eV exhibits the binding energy between the COF and the CNF. Although the value is higher compared to pristine CNF C1s (284.5 eV), **DqTp-CNF** displays a noticeable lower binding energy shift compared to the pristine **DqTp** COF (285.4 eV). The plausible reason behind this phenomenon could be the presence of the more electrophilic anthraquinone linkers in **DqTp** compared to the **DqDaTp** COF. In the **DqDaTp-CNF** hybrid, the anthracene as well as anthraquinone rich COF, and the graphene layer can actively donate as well as accept π-electrons due to the anthracene and anthraquinone functionalities respectively during the interlayer interaction. On the other hand, in the case of **DqTp**, the COF is more willing to accept, rather than donate, the electrons from the graphene layers due to the presence of electrophilic C=O moieties in anthraquinone. It is well documented that, the graphene layers are amenable to accept or donate or partially share their π-electrons, depending on the electronic property of the neighbouring counter molecules.[52-54] Moreover, the broad peak associated at ~287.7 eV (**DqDaTp-CNF**) and 286.0 eV (**DqTp-CNF**) correspond to the C1s of the C=O linkages. In addition, we could observe the noticeable binding energy shifts in the N1s XPS profile of the COF-CNF hybrid compared to the pristine COF (Supporting Information, Figure

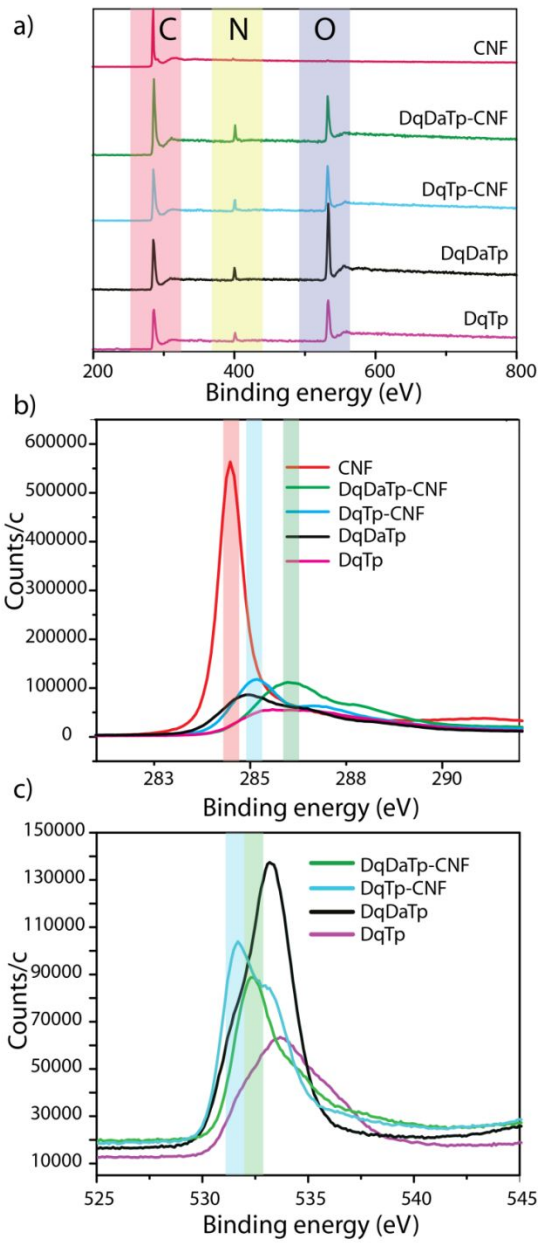

Figure 3: a) XPS profile (C, N, O) of COFs and COF-CNF hybrids; XPS peaks of b) C 1s; and c) O 1s.

S26). In the hetero-linked COF (**DqDaTp**), the N1s binding energy is shifted from 400.0 eV (pristine) to 400.5 eV (in the hybrid). Additionally, a small higher binding energy shift is perceptible in the case of **DqTp** (400.5 eV) to **DqTp-CNF** (400.7 eV). The O1s binding energy profile indicates a lowering in the binding energy for all COF-CNF hybrids (532.2 and 531.5 eV

for **DqTp-CNF** and **DqDaTp-CNF** respectively) compared to the pristine COF (533.7 and 533.2 eV for **DqTp** and **DqDaTp** respectively), which reflects an efficient interaction and subsequent withdrawal of the electrons from the CNF graphene layers (Figure 3a & c; Supporting Information, Figure S26).

The fabricated COF-CNF hybrids displayed a smooth surface with large areal synthetic scalability and good porosity (>16 cm^2) (Figure 4a, b & d; Supporting Information, Figure S1). The TEM imaging of the **DqTp-CNF** and **DqDaTp-CNF** hybrids showed an aggregated planar ribbon like assembly of the COF crystallites on the surface of the 70-80 nm fibrillar CNF (Figure 4f and g; Supporting Information, Figure S20 & Figure S49). Due to the larger diameter of the CNF (70-80 nm), it can accommodate the nano-crystalline COFs on the inner and the outer surface. We surmise that the preliminary growth of the COF crystallites on these CNF graphene layers because of interlayer π•••π interactions.[24-30] However, a simple physical mixture of COF and CNF could only display the presence of distinct entities, as evidenced from the TEM images (Supporting Information, Figure S22). This further suggests the necessity of *in situ* COF growth for the proper building of the COF-CNF hybrid material. The vertical cross-sectional SEM images of the **DqTp-CNF** and **DqDaTp-CNF** hybrids validate its uniform thickness (`~50 μm) (Figure 4h-k; Supporting Information, Figure S23-S24). SEM imaging Again, the top surface revealed that the crack-free nature of all the COF-CNF hybrids. Additionally, the cross-sectional imaging clearly shows the presence of CNF as a fibrillar morphology embedded in the COF matrix (Figure 4j and k). It is worth mentioning that the structural integrity and the flexibility of the COF-CNF hybrids primarily originate from the tight-binding between COF and CNF. This tight-binding between the COF and CNF remains intact even under prolonged ultrasonication and heating in highly polar solvents.

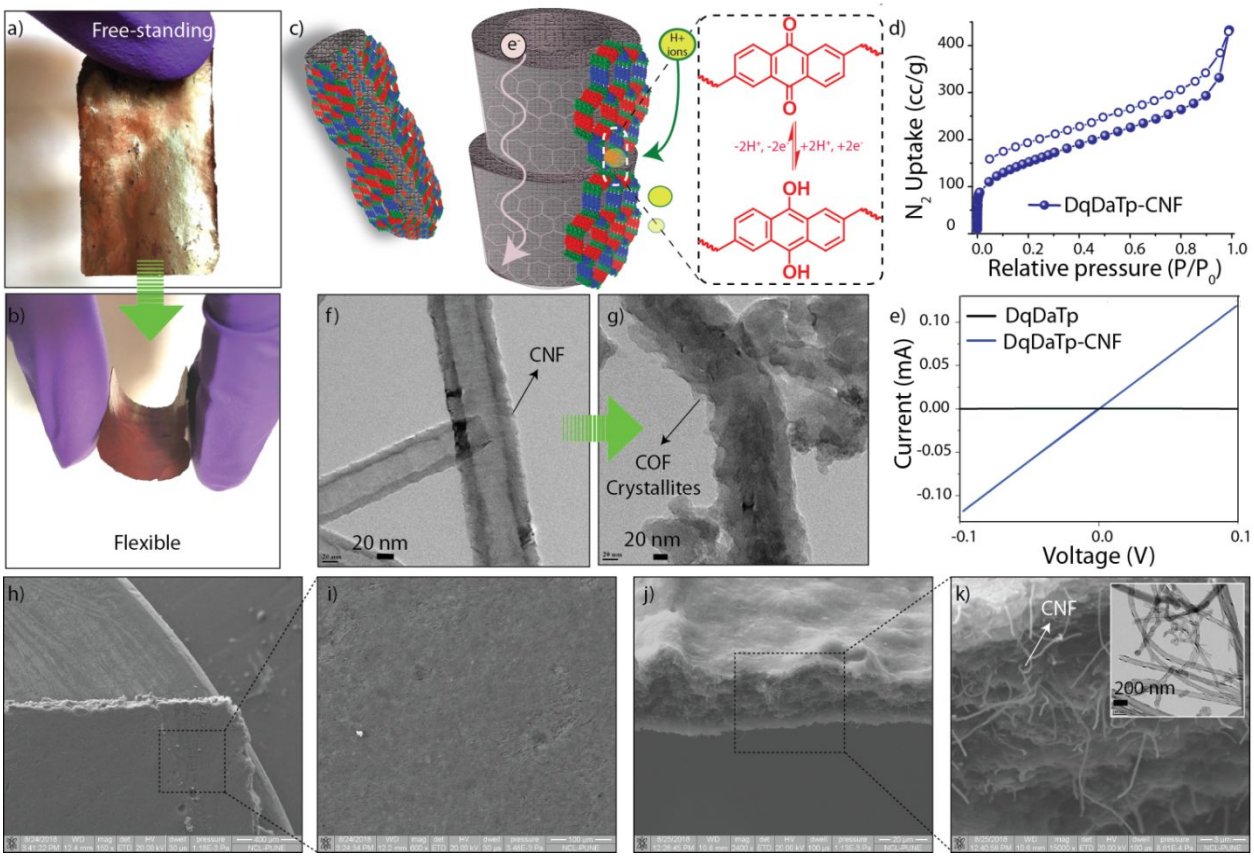

Figure 4: a & b) Photograph of free-standing and flexible **DqDaTp-CNF** hybrid thin sheet; c) Diagrammatic representation of COF-CNF hybrid model; d) N_2 adsorption isotherm analysis of **DqDaTp-CNF**; e) Current-Voltage relationship; TEM image of f) CNF and g) **DqDaTp-CNF**; SEM images of **DqDaTp-CNF** h & i) horizontal view; j & k) cross sectional view.

We anticipated that this interlayer π•••π interactions in the COF-CNF hybrid would improve the efficacy of the electron transfer in the matrix (Figure 4c). Moreover, the solid-state synthesis of the hybrid allows the construction of a free-standing thin sheet form, which provides an effective platform for bulk electronic conductivity. All the COF-CNF hybrids, including the pristine **DqTp** and **DqDaTp** COFs were subjected to a current-voltage (I-V) analysis to measure the electrical conductivity of the material (Figure 4e; Supporting Information, Figure S27). The I-V characteristics display the excellent electrical conductivity of 2.5×10^{-4} and 5.2×10^{-5} Scm^{-1} for the **DqTp-CNF** and **DqDaTp-CNF** hybrids respectively. However, the pristine **DqTp** and

DqDaTp COFs show high electrical resistance in the I-V plot (>10^{-14}Scm^{-1}). Therefore, we believe that the significant interlayer interaction between the redox active COF and the electron carrier graphene can bring an effective concurrent functioning of both activities during the electrochemical redox reaction. Hence, we have investigated the electrochemical performance of all COF-CNF hybrids considering a three-electrode assembly (Figure 5c; Supporting Information, S-10). We have measured the electrochemical impedance analysis of both COF-CNF hybrids and found that low equivalent series resistance (ESR) value ~2Ω (Figure S28 & S29). The cyclic voltammetry (CV, -O.5V to 05V) (Figure 5a, b; Supporting Information, Figure S30-S33) analysis of **DqTp-CNF** and **DqDaTp-CNF** hybrids showed significantly higher current response compared to the pristine **DqTp** and **DqDaTp** COFs. The effective utilization of charge storage sites has been improved dramatically in the hybrids owing to its porosity and higher electrical conductivity, which in turn exhibit a large enhancement of electrochemical energy storage. The areal capacitances of the hybrids were calculated by the galvanostatic charge-discharge experiment (GCDC) (Figure 5d & e; Supporting Information, Figure S34-S37 & S41). We have measured the IR drop values of the discharge curve of COF-CNF hybrids and pristine COFs. The slightly higher IR drops in the pristine compared to the hybrids could be due to the higher resistance of the COFs (Figure 5d & e). From GCDC, the areal capacitances of **DqTp-CNF** (464 mFcm^{-2}), and **DqDaTp-CNF (**364 mFcm^{-2}) hybrids have been evaluated at a current density of 0.25 mAcm^{-2}. It is worth mentioning that, the industrial standard requires a higher thickness of ~30-100 μm for the free-standing electrodes to be used in energy storage systems. In this regard, despite of the higher thicknesses (50 μm; following the industrial standard for a commercial electrode) [55, 56] in current study, compared to the substrate (Au)

supported COF thin films (~1 μm), **DqTp-CNF** and **DqDaTp-CNF** exhibit good volumetric

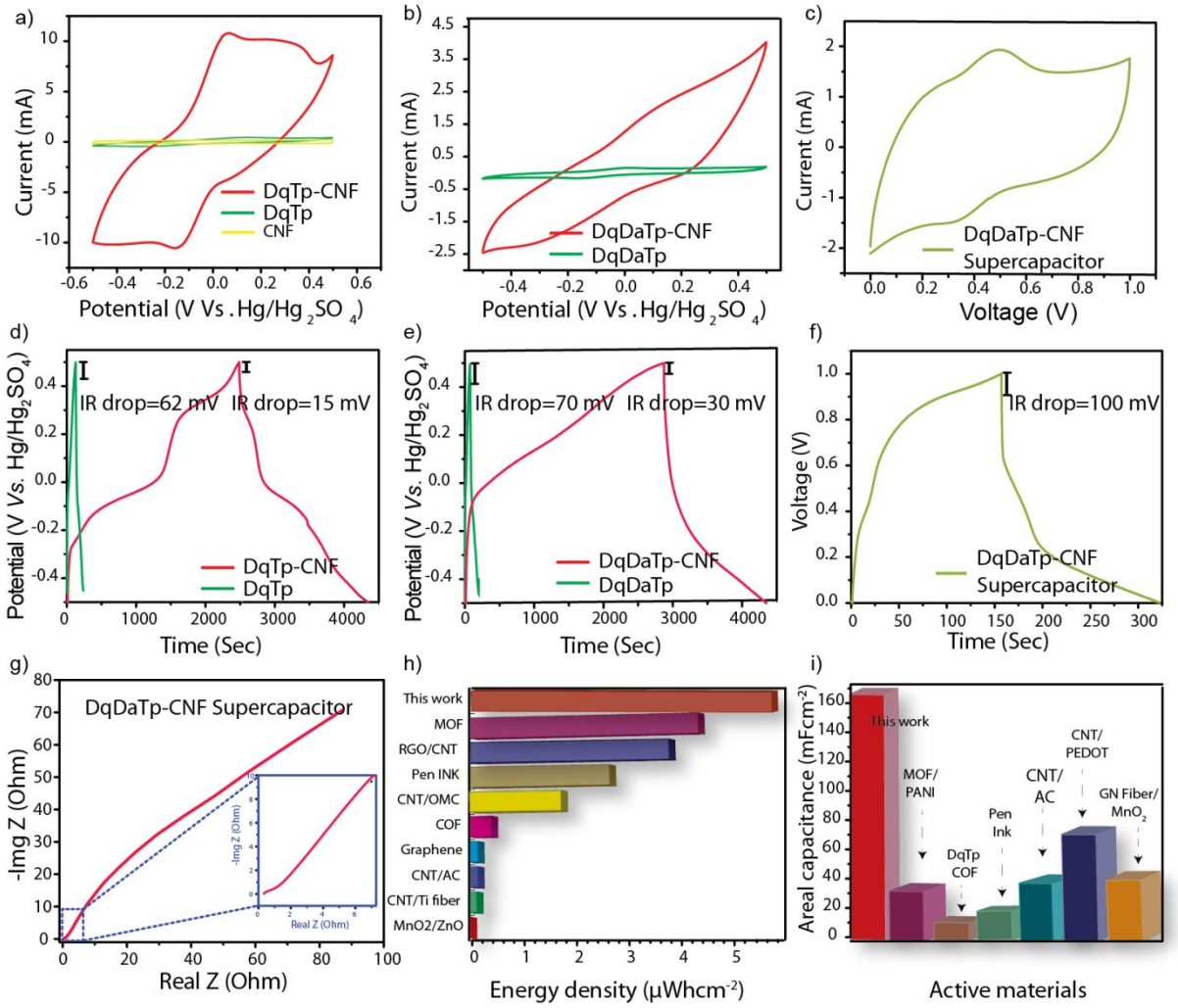

Figure 5: Cyclic voltammetry of a) **DqTp-CNF**; b) **DqDaTp-CNF** hybrids at 50 mVsec^{-1}; c) **DqDaTp-CNF** supercapacitor at 50 mVsec^{-1}; GCDC of d) **DqTp-CNF** at 0.25 mAcm^{-2}; e) **DqDaTp-CNF** at 0.25 mAcm^{-2}; f) **DqDaTp-CNF** supercapacitor at 0.5 mAcm^{-2}; g) Impedance profile; h) Comparison of energy density; and i) areal capacitance of the **DqDaTp-CNF** supercapacitor with the previous reports.

capacitances of 92.8 and 72.8 Fcm^{-3} respectively.[18, 55] On the other hand, the pristine **DqTp** and **DqDaTp** COFs could only deliver the capacitance values of 38 and 28 mFcm^{-2} respectively at the same current density which is signifying their insulating nature. Meanwhile, a negligible capacitance contribution (3 mFcm^{-2} at 0.25 mAcm^{-2}) has been noted from the GCDC of the CNF

by coating 1 mgcm^{-2} on a carbon paper (Supporting Information, Figure S38a). It indicates the role of CNF in the hybrids is limited only for carrying the electrons through the matrix. In addition, the physical mixture of **DqTp** COF and CNF displays a poor electrochemical performance (6.25 mFcm^{-2} at 0.25 mAcm^{-2}) due to the lack of effective π•••π interactions (Supporting Information, Figure S38b). In the pristine COF, although precisely integrated nano-pores assist to improve the electrolyte-electrode contact, the restricted electronic movements through the matrix lower the overall capacitance performance. Meanwhile, in COF-CNF hybrids, long channel electronic movement is feasible due to the intermolecular interactions between the COF and CNF layers. Here, the CNF facilitates electron transport through the sp^2 C=C framework. Moreover, higher electronic movement subsequently enhances the efficient utilization of redox-active centers, which in turn leads to an excellent electrochemical energy storage performance in the hybrids.

Although the electrochemical performance of the **DqTp-CNF** hybrid is excellent due to its high redox activity, the poor mechanical strength of the hybrid thin sheet inhibits its further utilization in a flexible electrochemical device. The dynamic mechanic analysis (DMA) of the **DqTp-CNF** hybrid yields a breaking strain of only 1.2% as evaluated from the stress-strain plot (Supporting Information, Figure S25). Whereas, the hetero-linked **DqDaTp-CNF** exhibits excellent mechanical properties (breaking strain: 5.8%) due to the presence of anthracene moieties.[32] Therefore, considering the advantage of both decent mechanical strength and the electrochemical energy storage performance, we decided to fabricate a symmetric quasi-solid state supercapacitor based on the **DqDaTp-CNF** hybrid as electrodes and PVA/H_2SO_4 gel as an electrolyte. The impedance analysis displays the ESR value is 0.2 Ω (Figure 5g). The redox waves in the CV profile (potential window of 1V) of the device clearly indicated the redox

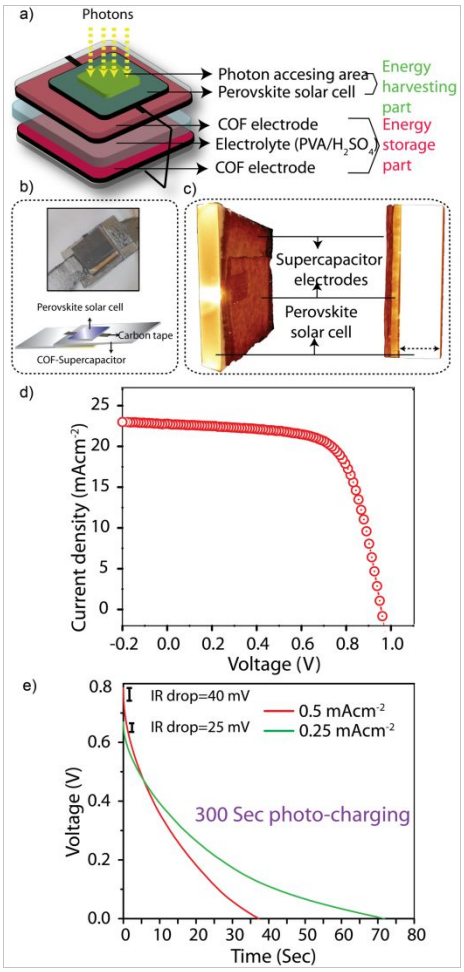

Figure 6: a) A diagrammatic representation of PSC; b) Photograph of PSC as a wearable device and the diagrammatic representation of the supercapacitor; c) X-ray tomography 3D image displays the interphases of the device; d) Voltage-current density curve of the perovskite solar cell; e) Discharging of the photo charged supercapacitor device.

behavior of the anthraquinone moiety (Figure 5c; Supporting Information, Figure S39). From GCDC, the areal capacitance for the device was calculated to be 167 $mFcm^{-2}$ at a current density of 0.5 $mAcm^{-2}$ (Figure 5f; Supporting Information, Figure S40). Notably, to the best of our knowledge, the device areal capacitance is one of the best values achieved among MOFs, COFs and several other carbon-based supercapacitor devices (Figure 5h; Supporting Information, Table S2).[33-38] Moreover, we determined the cyclic stability of the device at a current density of 5 $mAcm^{-2}$ which display 76% of capacitance retention even after 4500 continuous charge-

discharge cycles (Supporting Information, Figure S43). The **DqDaTp-CNF** hybrid also exhibits unprecedented areal energy density (***Ea***) as high as 5.8 μWhcm^{-2} at 0.5 mAcm^{-2} (Figure 5i; Supporting Information, Figure S42). Additionally, at the same current density, it delivers the areal power density (***Pa***) of 125.0 μWcm^{-2}. Furthermore, in order to attain the concurrent green energy harvesting and its subsequent storage, herein, for the first time, we have fabricated a COF supercapacitor based self-charging power-pack. In this photovoltaic charged device, the **DqDaTp-CNF** based supercapacitor is integrated with a highly efficient perovskite solar cell with the power conversion efficiency of 16.7% (Figure 6a,b, c, & d; Supporting Information, S-11, Figure S44-S46). Under the solar simulator illumination (0.88Sun), the solar cell converts the photon energy to the electrical energy, which efficiently charged the **DqDaTp-CNF** supercapacitor bearing the active area of 1.0 cm^2. We observed that the supercapacitor device attained a large photo-charge voltage of 0.8 V within 100 seconds as measured using a multimeter. Notably, in our present study, we have charged the integrated device photovoltaically for 100, 200 and 300 seconds and have measured the galvanostatic discharging time of the respective supercapacitor after disconnecting from the monolithic device (Figure 6e; Supporting Information, Figure S45). Herein, we noticed that the discharging time was increasing with the time of photovoltaic charging, which signifies the practical usage of the designed self-power pack as a real-life device for the uptake of solar energy and the further operation in wearable electronics (Supporting Information, Figure S44). We measured the discharging time by varying current densities (0.25 and 0.5 mAcm^{-2}) to calculate the delivered areal capacitance of the device. For the 300 seconds photo-charging, we obtained 42.0 mFcm^{-2} areal capacitance at the current density of 0.25 mAcm^{-2}, which compares well with the reported solar cell-supercapacitor based integrated devices (Table S3).[39-42]

Conclusion

In summary, we have demonstrated a facile strategy to enhance the electrical conductivity of the COF thin-sheet by the *in situ* solid-state inclusion of the carbon nanofiber into the COF precursor matrix. The obtained COF-CNF hybrids exhibit crystalline and porous nature along with the enhanced electrical conductivity. The weak intermolecular interaction of COF and graphene layers in CNF aids the strong alignment of the hybrid, which further displays a large betterment in the areal capacitance (464 $mFcm^{-2}$) from the pristine COF (38 $mFcm^{-2}$). Also, the fabricated solid-state COF supercapacitor displays high performance (167 $mFcm^{-2}$) in electrochemical energy storage. As a proof of concept, we have integrated a self power-pack based on the COF supercapacitor and a perovskite solar cell by a monolithic assembling through adhesive carbon tape. The fabricated device displays a fair discharging time and the areal capacitance of the supercapacitor holds 42.0 $mFcm^{-2}$.

ASSOCIATED CONTENT

Supporting Information.

Full experimental procedures and characterization dataare available as a separate file (PDF).

AUTHOR INFORMATION

Corresponding Author

* *r.banerjee@ncl.res.in*

ORCID

Abdul khayum Mohammed: 0000-0001-8626-1751
Vidyanand Vijayakumar: 0000-0001-6061-5902
Arjun Halder: 0000-0001-0400-6592
Meena Ghosh: 0000-0001-9068-719X
Matthew Addicoat: 0000-0002-5406-7927
Sreekumar Kurungot: 0000-0001-5446-7923
Rahul Banerjee: 0000-0002-3547-4746

ACKNOWLEDGMENT

A.K.M &V.V acknowledge UGC Govt. of India for Senior Research Fellowship. A.H & M.G. acknowledge CSIR, Govt. of India for Senior Research Fellowship. M.A.A. thanks the Materials Chemistry Consortium for computational resources on THOMAS (EP/P020194). S.K. acknowledges CSIR-New Delhi for the project TLP003526. R.B. acknowledges IISER-Kolkata Startup grant and Swarna Jayanti Fellowship grant [DST/SJF/CSA-02/2016-2017] for funding and Carl Friedrich von Siemens Research Fellowship and the Alexander von Humboldt Foundation. We acknowledge Dr. T. G. Ajith Kumar for providing NMR, Fayiz K. P and Dr. M. V Badiger for X-ray tomography and Dr. G. Kumaraswamy for PXRD facility.

REFERENCES

1. Cote, A. P.; Benin, A. I.; Ockwig, N. W.; Matzger, A. J.; O'Keeffe, M.; Yaghi, O. M. Porous, Crystalline, Covalent Organic Frameworks. *Science* **2005**, *310*, 1166-1170.

2. Kuhn, P.; Antonietti, M.; Thomas, A. Porous, Covalent Triazine Based Frameworks Prepared by Ionothermal Synthesis. *Angew. Chem. Int. Ed.* **2008**, *47*, 3450-3453.

3. Ding, S.-Y.; Wang, W. Covalent Organic Frameworks (COFs): from Design to Applications. *Chem. Soc. Rev.* **2013**, *42*, 548-568.

4. Wang, S.; Wang, Q.; Shao, P.; Han, Y.; Gao, X.; Ma, L.; Yuan, S.; Ma, X.; Zhou, J.; Feng, X.; Wang, B. Exfoliation of Covalent Organic Frameworks into Few-Layer Redox-Active Nanosheets as Cathode Materials for Lithium-Ion Batteries. *J. Am. Chem. Soc.* **2017**, *139*, 4258-4261.

5. Crowe, J. W.; Baldwin, L. A.; McGrier, P. L. Luminescent Covalent Organic Frameworks Containing a Homogeneous and Heterogeneous Distribution of Dehydrobenzoannulene Vertex Units *J. Am. Chem. Soc*. **2016**, *138*, 10120-10123.

6. Sun, A.; Aguila, B.; Perman, J.; Nguyen, N.; Ma, S. Flexibility Matters: Cooperative Active Sites in Covalent Organic Framework and Threaded Ionic Polymer. *J. Am. Chem. Soc.* **2016**, *138*, 15790-15796.

7. Han, X.; Xia, Q.; Huang, J.; Liu, Y.; Tan, C.; Cui, Y. Salen-Based Covalent Organic Framework *J. Am. Chem. Soc*. **2017**, *139*, 8693-8697.

8. Liu, X-H.; Guan, C-Z.; Ding, S-Y.; Wang, W.; Yan, H-J.; Wang, D.; Wan, L-J. On-Surface Synthesis of Single-Layered Two-Dimensional Covalent Organic Frameworks via Solid–Vapor Interface Reactions. *J. Am. Chem. Soc*. **2013**, *135*, 10470-10474.

9. Dogru, M.; Sonnauer, A.; Gavryushin, A.; Knochel, P.; Bein, T. A Covalent Organic Framework with 4 nm Open Pores. *Chem. Commun*. **2011**, *47*, 1707-1709.

10. Stegbauer, L.; Schwinghammer, K.; Lotsch, B. V. A Hydrazone-Based Covalent Organic Framework for Photocatalytic Hydrogen Production. *Chem. Sci.* **2014**, *5*, 2789-2793.

11. Jin, E. Q.; Asada, M.; Xu, Q.; Dalapati, S.; Addicoat, M. A.; Brady, M. A.; Xu, H.; Nakamura, T.; Heine, T.; Chen, Q. H.; Jiang, D. L. Two-Dimensional sp2 Carbon–Conjugated Covalent Organic Frameworks. *Science* **2017**, *357*, 673-676.

12. DeBlase, C. R.; Silberstein, K. E.; Truong, T. T.; Abruna, H. D.; Dichtel, W. R. β-Ketoenamine-Linked Covalent Organic Frameworks Capable of Pseudocapacitive Energy Storage. *J. Am. Chem. Soc.* **2013**, *135*, 16821-16824.

13. DeBlase, C. R.; Hernandez-Burgos, K.; Silberstein, K. E.; Rodriguez-Calero, G. G.; Bisbey, R. P.; Abruna, H. D.; Dichtel, W. R. Rapid and Efficient Redox Processes within 2D Covalent Organic Thin Films. *ACS Nano* **2015**, *9*, 3178-3183.

14. Khattak, A. M.; Ghazi, Z. A.; Liang, B.; Khan, N. A.; Iqbal, A.; Li, L.; Tang, Z. A Redox-Active 2D Covalent Organic Framework with Pyridine Moieties Capable of Faradaic Energy Storage. *J. Mater. Chem. A* **2016**, *4*, 16312-16317.

15. Wang, F.; Wu, X.; Yuan, X.; Liu, Z.; Zhang, Y.; Fu, L.; Zhu, Y.; Zhou, Q.; Wu, Y.; Huang, W. Latest Advances in Supercapacitors: from New Electrode Materials to Novel Device Designs. *Chem. Soc. Rev.* **2017**, *46*, 6816-6854.

16. Chandra, S.; Roy Chowdhury, D.; Addicoat, M.; Heine, T.; Paul, A.; Banerjee, R. Molecular Level Control of the Capacitance of Two Dimensional Covalent Organic Frameworks: Role of Hydrogen Bonding in Energy Storage Materials. *Chem. Mater.* **2017**, *29*, 2074-2080.

17. Zhou, J.; Wang, B. Emerging Crystalline Porous Materials as a Multifunctional Platform for Electrochemical Energy Storage. *Chem. Soc. Rev.* **2017**, *46*, 6927-6945.

18. Mulzer, C. R.; Shen, L.; Bisbey, R. P.; McKone, J. R.; Zhang,N.; Abruña, H. D.; Dichtel, W. R. Superior Charge Storage and Power Density of a Conducting Polymer-Modified Covalent Organic Framework *ACS Cent. Sci*. **2016**, *2,* 667−673.

19. Zha, Z.; Xu, L.; Wang, Z.; Li, X.; Pan, Q.; Hu, P.; Lei, S. 3D Graphene Functionalized by Covalent Organic Framework Thin Film as Capacitive Electrode in Alkaline Media. *ACS Appl. Mater. Interfaces* **2015**, *7*, 17837−17843.

20. Lei, Z.; Yang, Q.; Xu, Y.; Guo, S.; Sun, W.; Liu, H.; Lv, L.-P.; Zhang, Y.; Wang, Y. Boosting Lithium Storage in Covalent Organic Framework via Activation of 14-Electron Redox Chemistry. *Nat. Commun*. **2018**, *9*, 576.

21. Chen, X.; Zhang, H.; Ci, C.; Sun, W.; Wang, Y. Few-Layered Boronic Ester Based Covalent Organic Frameworks/Carbon Nanotube Composites for High-Performance K‑Organic Batteries, *ACS Nano* **2019**, *13*, 3600−3607

22. Feng, L.; Xie, N.; Zhong, J. Carbon Nanofibers and Their Composites: A Review of Synthesizing, Properties and Applications. *Materials* **2014**, *7*, 3919–3945.

23. Karak, S.; Kandambeth, S.; Biswal, B. P.; Sasmal, H. S.; Kumar, S.; Pachfule, P.; Banerjee, R. Constructing Ultraporous Covalent Organic Frameworks in Seconds via an Organic Terracotta Process. *J. Am. Chem. Soc*. **2017**, *139*, 1856-1862.

24. Hunter, C. A.; Sanders, J. K. M. The Nature of .Pi.-.Pi.Interactions. *J. Am. Chem. Soc.* **1990**, *112*, 5525-5534.

25. Müller-Dethlefs, K.; Hobza, P. Noncovalent Interactions: A Challenge for Experiment and Theory *Chem. ReV.***2000**, *100*, 143-168.

26. Perez, E. M.; Martin, N. π–π Interactions in Carbon Nanostructures. *Chem. Soc. Rev*. **2015**, *44*, 6425-6433.

27. Desiraju, G. R.; Steiner, T. The Weak Hydrogen Bond; Oxford University Press: New York, **1999**.

28. Desiraju, G. R. The C− H···O Hydrogen Bond: Structural Implications and Supramolecular Design. *Acc. Chem. Res.* **1996**, *29*, 441-449.

29. Steiner, T.; Desiraju, G. R. Distinction between The Weak Hydrogen Bond and the Van der Waals Interaction. *Chem. Commun*. **1998**, *8*, 891-892.

30. Wang, W.; Zhang, Y.; Wang, Y. B. Noncovalent π···π Interaction between Graphene and Aromatic Molecule: Structure, Energy, and Nature. *J. Chem. Phys*. **2014**, *140* (094302), 1−6

31. Kandambeth, S.; Mallick, A.; Lukose, B.; Mane, M. V.; Heine, T.; Banerjee, R. Construction of Crystalline 2D Covalent Organic Frameworks with Remarkable Chemical (Acid/Base) Stability via a Combined Reversible and Irreversible Route. *J. Am. Chem. Soc.* **2012**, *134*, 19524-19527.

32. M, A. K,; Vijayakumar. V.; Karak, S.; Kandambeth, S.; Bhadra, M.; Suresh, K.; Acharambath, N.; Kurungot, S.; Banerjee, R. Convergent Covalent Organic Framework

Thin Sheets as Flexible Supercapacitor Electrodes. *ACS Appl. Mater. Interfaces*, **2018**, *10*, *33,* 28139–28146.

33. Wang, L.; Feng, X.; Ren, L.; Piao, Q.; Zhong, J.; Wang, Y.; Li, H.; Chen, Y.; Wang, B. Flexible Solid-State Supercapacitor Based on a Metal-Organic Framework Interwoven by Electrochemically-Deposited PANI. *J. Am. Chem. Soc.* **2015**, *137*, 4920−4923.

34. Fu, D.; Zhou, H.; Zhang, X.-M.; Han, G.; Chang, Y.; Li, H. Flexible Solid-state Supercapacitor of Metal-Organic Framework Coated on Carbon Nanotube Film Interconnected by Electrochemically-codeposited PEDOT-GO. *Chemistry Select* **2016**, *1*, 285−289.

35. Qi, K.; Hou, R.; Zaman, S.; Qiu, Y.; Xia, B. Y.; Duan, H. Construction of Metal-Organic Framework/Conductive Polymer Hybrid for All-Solid-State Fabric Supercapacitor. *ACS Appl. Mater. Interfaces* **2018**, *10*, 18021−18028.

36. Fu, Y.; Cai, X.; Wu, H.; Lv, Z.; Hou, S.; Peng, M.; Yu, X.; Zou, D. Fiber Supercapacitors Utilizing Pen Ink for Flexible/Wearable Energy Storage. *Adv. Mater*. **2012**, *24*, 5713–5718.

37. Wang, K.; Meng, Q.; Zhang, Y.; Wei, Z.; Miao, M. High PerformanceTwo-Ply Yarn Supercapacitors Based on Carbon Nanotubes and Polyaniline Nanowire Arrays. *Adv. Mater.* **2013**, *25*, 1494–1498.

38. Dong, L.; Xu, C.; Li, Y.; Huang, Z. H.; Kang, F.; Yang, Q. H.; Zhao, X. Flexible Electrodes and Supercapacitors for Wearable Energy Storage: A Review by Category. *J. Mater. Chem. A* **2016**, *4*, 4659− 4685.

39. Guo, W. X.; Xue, X. Y.; Wang, S. H.; Lin, C. J.; Wang, Z. L. An Integrated Power Pack of Dye-Sensitized Solar Cell and Li Battery Based on Double-Sided TiO2 Nanotube Arrays. *Nano Lett*. **2012**, *12*, 2520-2523.

40. Zhang, Z.; Chen, X.; Chen, P.; Guan, G.; Qiu, L.; Lin, H.; Yang, Z.; Bai, W.; Luo, Y.; Peng, H. Integrated Polymer Solar Cell and Electrochemical Supercapacitor in a Flexible and Stable Fiber Format. *Adv. Mater*. **2014**, *26*, 466-470.

41. Xu, X.; Li, S.; Zhang, H.; Shen, Y.; Zakeeruddin, S. M.; Graetzel, M.; Cheng, Y.-B.; Wang, M. A. Power Pack Based on Organometallic Perovskite Solar Cell and Supercapacitor. *ACS Nano* **2015**, *9*, 1782−1787.

42. Kim, J.; Lee, S. M.; Hwang, Y.-H.; Lee, S.; Park, B.; Jangac, J.-H.; Lee, K. A Highly Efficient Self-power Pack System Integrating Supercapacitors and Photovoltaics with an Area-saving Monolithic Architecture. *J. Mater. Chem. A*, **2017**, *5*, 1906-1912.

43. Georgakilas, V.; Tiwari, J. N.; Kemp, K. C.; Perman, J. A.; Bourlinos, A. B.; Kim, K. S.; Zboril, R. Noncovalent Functionalization of Graphene and Graphene Oxide for Energy Materials, Biosensing. Catalytic, and Biomedical Applications. *Chem. Rev.***2016**, *116*, 5464-5519.

44. Chen, D.; Feng, H.; Li, J. Graphene Oxide: Preparation, Functionalization, and Electrochemical Applications. *Chem. Rev*. **2012**, *112*, 6027-6053.

45. Stankovich, S.; Dikin, D. A.; Dommett, G. H. B.; Kohlhaas, K. M.; Zimney, E. J.; Stach, E. A.; Piner, R. D.; Nguyen, S. T.; Ruoff, R. S. Graphene-Based Composite Materials. *Nature* **2006**, *442*, 282-286.

46. Gunasinghe, R. N.; Reuven, D. G.; Suggs, K.; Wang, X.-Q. Filled and Empty Orbital Interactions in a Planar Covalent Organic Framework on Graphene. *J. Phys. Chem. Lett*. **2012**, *3*, 3048−3052.

47. Xu, L.; Zhou, X.; Tian, W. Q.; Gao, T.; Zhang, Y. F.; Lei, S.; Liu, Z. F. Surface-Confined Single-Layer Covalent Organic Framework on Single-Layer Graphene Grown on Copper Foil. *Angew. Chem., Int. Ed.* **2014**, *53*, 9564−9568.

48. Usachov, D.; Vilkov, O.; Gruneis, A.; Haberer, D.; Fedorov, A.; Adamchuk, V. K.; Preobrajenski, A. B.; Dudin, P.; Barinov, A.; Oehzelt, M.; Laubschat, C.; Vyalikh, D. V. Nitrogen-Doped Graphene: Efficient Growth, Structure, and Electronic Properties, *Nano Lett.* **2011**, *11*, 5401−5407.

49. Guo, J.; Lin, C.-Y.; Xia, Z.; Xiang, Z. A Pyrolysis-Free Covalent Organic Polymer for Oxygen Reduction. *Angew. Chem. Int. Ed*., **2018**, *57*, 1–7.

50. Kabir, S.; Artyushkova, K.; Serov, A.; Kiefer, B.; Atanassov, P. Binding Energy Shifts for Nitrogen-Containing Graphene-Based Electrocatalysts - Experiment and DFT Calculations. *Surf. Interface Anal.* **2016**, *48*, 293–300.

51. Artyushkova, K.; Kiefer, B.; Halevi, B.; Knop-Gericke, A.; Schlogl, R.; Atanassov, P. Density Functional Theory Calculations of XPS Binding Energy Shift for Nitrogen-Containing Graphene-Like Structures, *Chem. Commun*. **2013**, *49*, 2539−2541.

52. Loh, K. P.; Bao, Q. L.; Ang, P. K.; Yang, J. X. The Chemistry of Graphene. *J. Mater. Chem*. **2010**, *20*, 2277-2289.

53. Stergiou, A.; Pagona, G.; Tagmatarchis, N. Donor−Acceptor Graphene-Based Hybrid Materials Facilitating Photo-Induced Electron-Transfer Reactions. Beilstein *J. Nanotechnol*. **2014**, *5*, 1580−1589.

54. Ragoussi, M. E.; Katsukis, G.; Roth, A.; Malig, J.; de la Torre, G.; Guldi, D. M.; Torres, T. Electron-Donating Behavior of Few-Layer Graphene in Covalent Ensembles with Electron-Accepting Phthalocyanines. *J. Am. Chem. Soc*. **2014**, *136*, 4593−4598.

55. Gogotsi, Y.; Simon, P. True Performance Metrics in Electrochemical Energy Storage. Science 2011, 334, 917–918.

56. Xia, Y.; Mathis, T. S.; Zhao, M.-Q.; Anasori, B.; Dang, A.; Zhou, Z.; Cho, H.; Gogotsi, Y.; Yang, S. Thickness-Independent Capacitance of Vertically Aligned Liquid-Crystalline MXenes. Nature 2018, 557, 409−412.

Table of Contents (TOC) Graphic

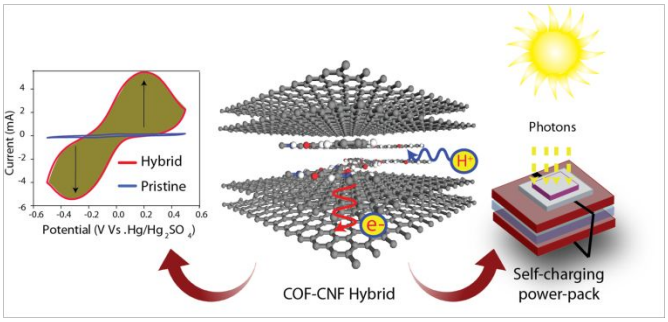

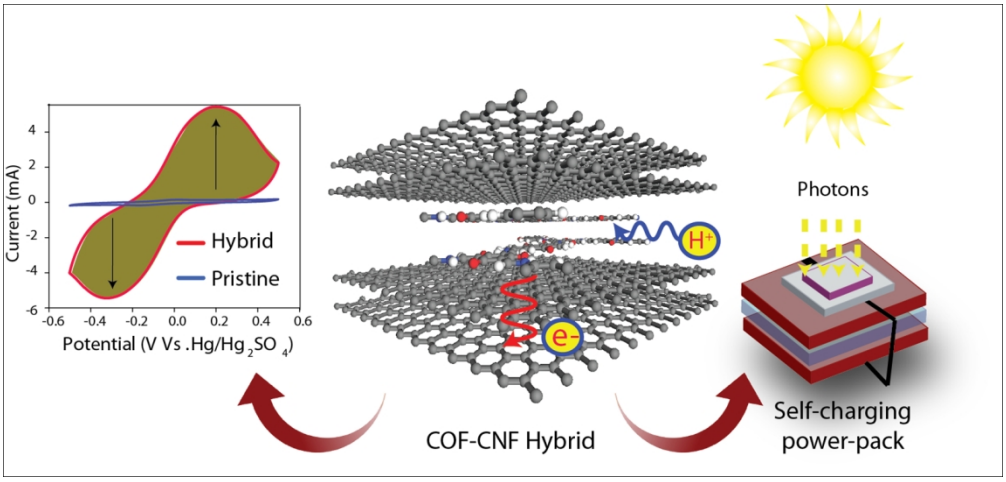

Figure_TOC

2301x1087mm (18 x 18 DPI)

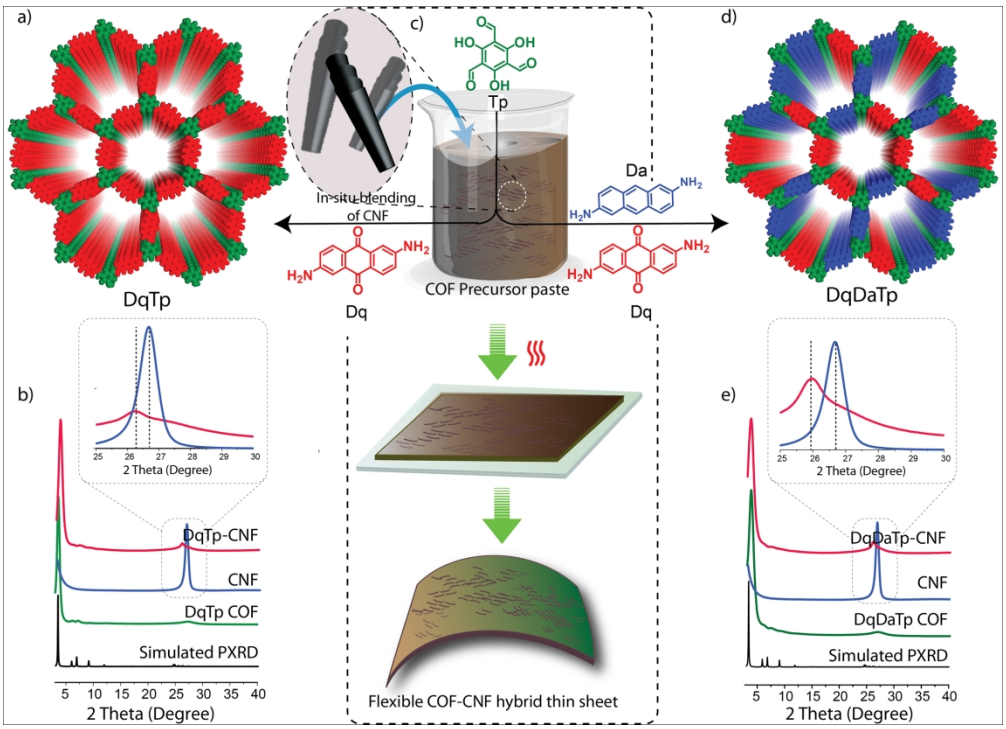

Figure 1

385x277mm (150 x 150 DPI)

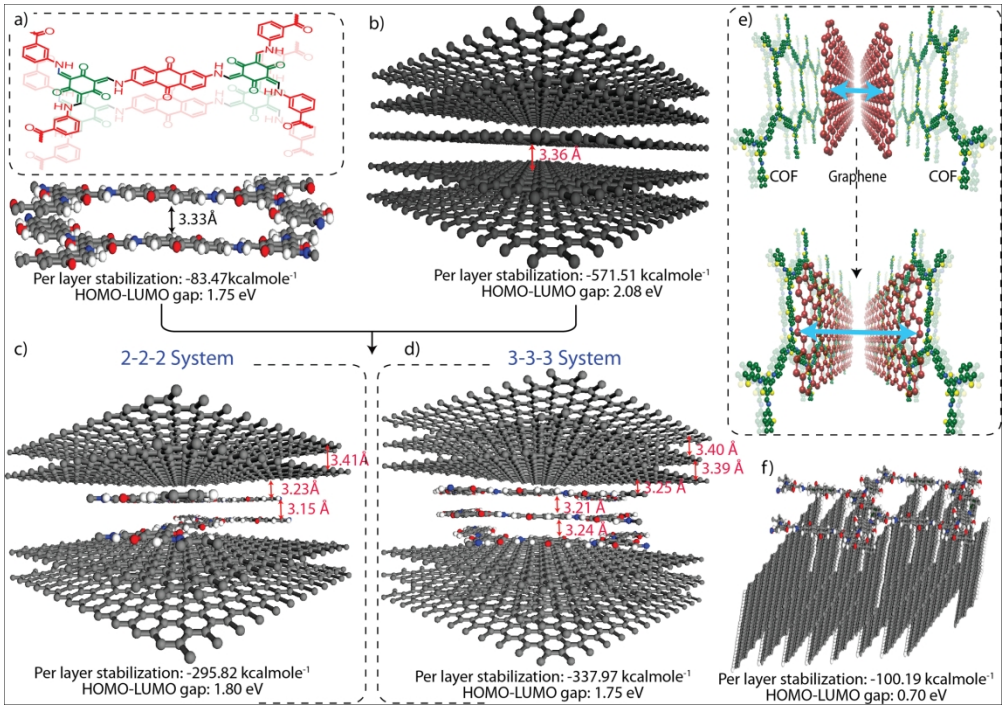

Figure 2

371x260mm (150 x 150 DPI)

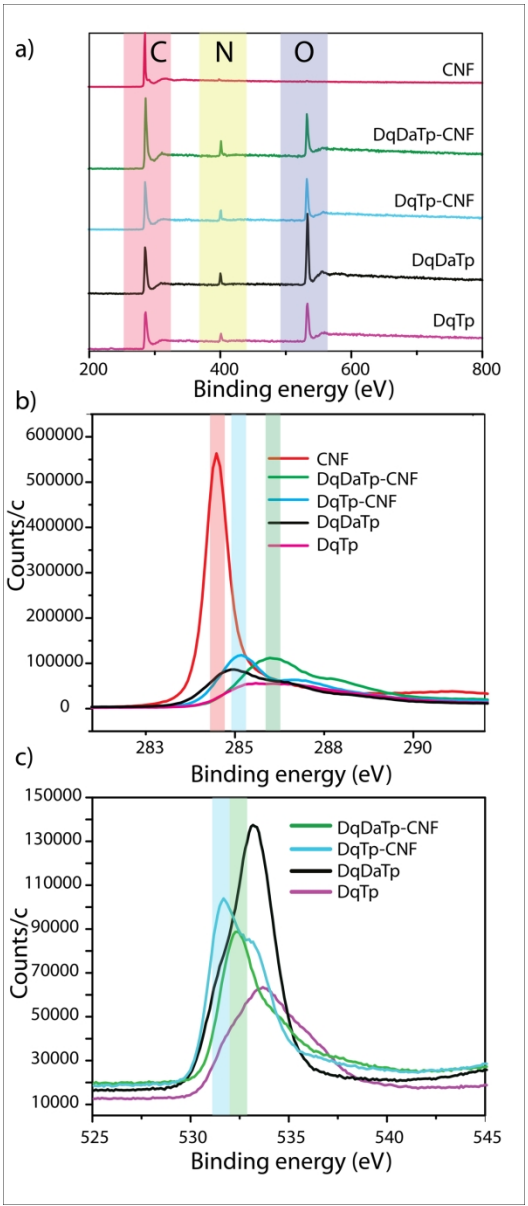

Figure 3

215x495mm (150 x 150 DPI)

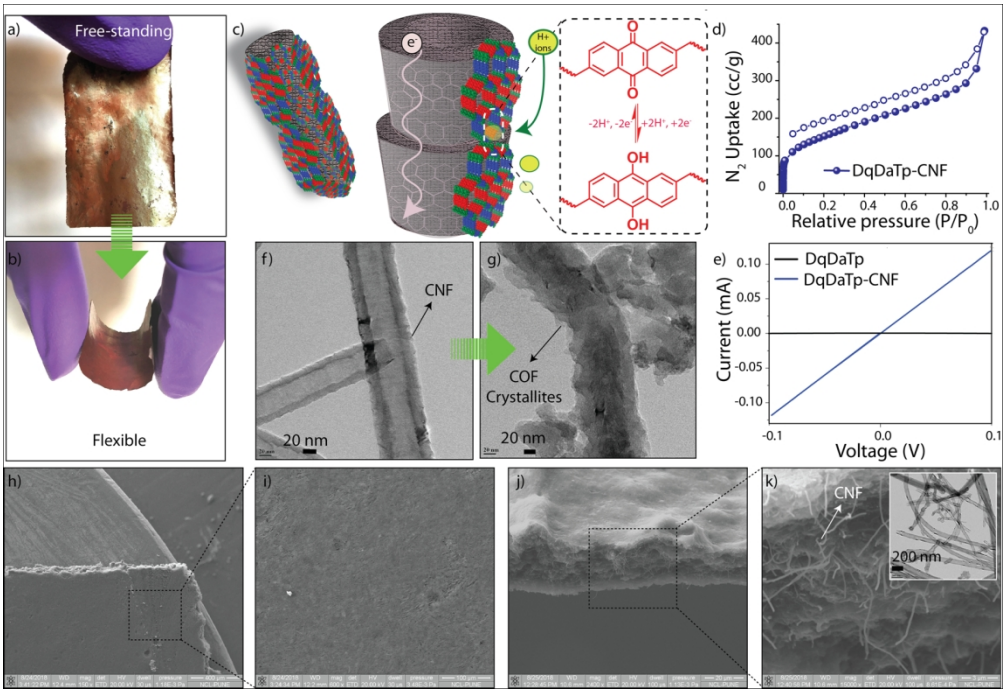

Figure 4

309x211mm (150 x 150 DPI)

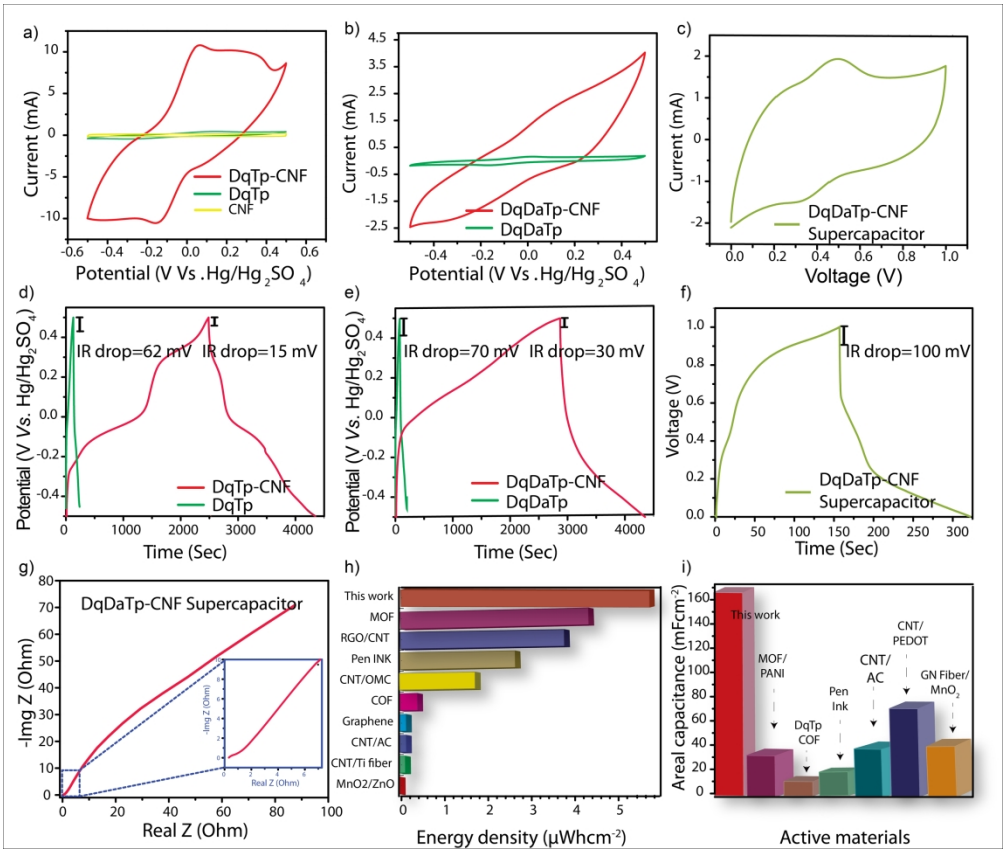

Figure 5

501x423mm (150 x 150 DPI)

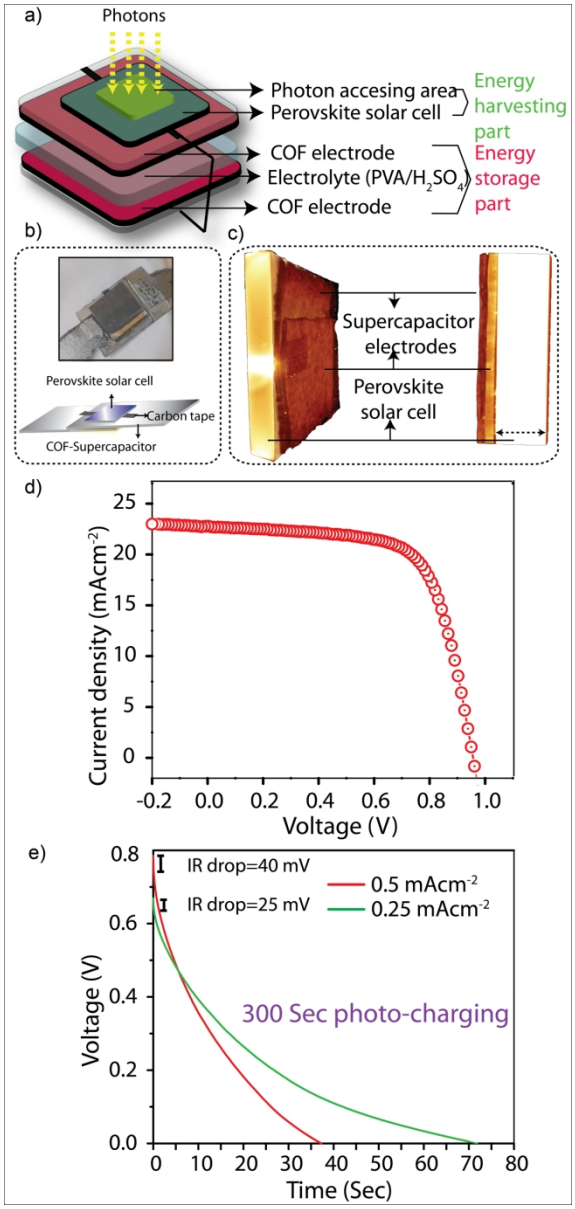

Figure 6

217x458mm (150 x 150 DPI)